scientific reports

OPEN

Quasi periodic photonic crystal as gamma detector using Poly nanocomposite and porous silicon

Fatma A. Sayed[1], May Bin-Jumah[2], Arafa H. Aly[1], V. D. Zhaketov[3,4], Mohammed Sallah[5] & Zaky A. Zaky[1,3,6]✉

This research investigates the design and performance of quasi-periodic photonic crystals built using Thue-Morse sequences for gamma dosimetry applications. The structures were made of aluminum oxide and porous silicon infused with a poly(ethylene oxide) nanocomposite. The transmittance spectra of these crystals are heavily dependent on their structural evolution, with higher-generation structures exhibiting greater localization of defect modes. The study combines experimental data fitting with theoretical calculations to validate the optical behavior of the developed structures. These calculations were performed using the transfer matrix method over a wavelength range of 500–800 nm. Each structure's sensitivity and quality factor were evaluated in two radiation ranges—0–100 Gy and 100–200 Gy—to determine their potential as gamma dosimeters. The results demonstrate that the proposed structures are highly effective for dosimetry applications. They achieve an optimal balance between sensitivity (0.55 nm/Gy and 0.5 nm/Gy) and sharp defect modes, with quality factors of 1715.9 and 473, respectively. These findings suggest that Thue-Morse sequence-based photonic crystals can serve as highly tunable and efficient gamma radiation sensors.

Keywords Porous silicon, Polymer nanocomposite, Quasi-periodic photonic crystal, Dosimeter

Gamma dosimeters play a critical role in measuring and monitoring ionizing radiation levels in diverse fields. They are indispensable in fields such as radiation therapy, the nuclear industry, medical diagnostics, and environmental monitoring[1]. Gamma radiation detection must be precise to ensure safety and optimize its application. Conventional dosimeters based on gamma radiation-induced physical and chemical changes include thermoluminescent dosimeters and optically stimulated luminescence dosimeters. To meet the rigorous demands of modern applications, there is a growing demand for advanced dosimetric materials that exhibit higher sensitivity, precision, and reliability[2].

A nanocomposite material comprises one or more nanoscale substances mixed with a bulk-phase material. Nanocomposites can be classified into three main types based on their matrix materials: ceramic matrix nanocomposites, metal matrix nanocomposites, and polymer matrix nanocomposites. A polymer or copolymer with nanoparticles or nanofillers dispersed within the polymer matrix constitutes a polymer nanocomposite. Nanocomposites, due to nanoscale fillers incorporated in a polymer matrix, have shown great promise as radiation-sensing materials because of their remarkable optical, electrical, and mechanical characteristics[2–4].

When nanocomposites interact with gamma radiation, the polymer's optical and structural properties, such as its absorption, photoluminescence, and refractive index, change. Due to its flexibility, chemical stability, and capacity to build nanocomposite structures, poly(ethylene oxide) (PEO), a widely studied polymer, is particularly suitable for such applications. PEO-based nanocomposites exhibit changes in optical transparency and structural organization upon gamma irradiation, enabling accurate dosimetric measurements. Owing to its exceptional properties, including chemical stability, heat resistance, and flexibility, PEO is widely used as a flexible polymer in various radiation-sensitive applications. PEO has been extensively researched for radiation-sensitive applications, such as gamma dosimeters, due to gamma radiation's significant impact on its optical and structural properties[5,6]. Furthermore, thermo-sensitive polymer gels have been investigated for their gamma

[1]Physics Department, Faculty of Sciences, TH-PPM Group, Beni-Suef University, Beni Suef 62514, Egypt. [2]Department of Biology, college of Science, Princess Nourah bint Abdulrahman University, P.O. BOX 84428, Riyadh 11671, Saudi Arabia. [3]Frank Laboratory of Neutron Physics, Joint Institute for Nuclear Research, Dubna 141980, Russia. [4]Moscow Institute of Physics and Technology (State University), Dolgoprudnyi, Moscow oblast, Russia. [5]Department of Physics, College of Sciences, University of Bisha, P.O. Box 344, Bisha 61922, Saudi Arabia. [6]Academy of Scientific Research and Technology (ASRT), Cairo, Egypt. ✉email: zaky.a.zaky@science.bsu.edu.eg; zaky@jinr.ru

sensitivity. These gels exhibit property changes such as color or optical clarity in response to gamma exposure, enabling visual detection. Specifically, reversible thermo-sensitive polymer gels have been proposed to enhance superheated emulsion (bubble) detectors by extending their operational temperature range and improving their gamma response[7].

Porous silicon (PSi) is a versatile material with excellent optical properties such as a large surface area, and tunable porosity. PSi is a popular choice for sensors, optoelectronics, and biomedical devices owing to these properties. PSi is highly sensitive to environmental changes, particularly to radiation effects, due to its extremely high surface-to-volume ratio. Furthermore, PSi's refractive index modulation under gamma radiation forms the basis for its application in photonic dosimeters, which requires precise optical responses[1,8,9].

Polymers and other materials can be incorporated into PSi's matrix thanks to its unique microstructure consisting of interconnected pores[9]. This enhances PSi's optical responsiveness to external stimuli. Gamma radiation exposure causes high-energy photons to interact with PSi, altering its refractive index. Ionization, atomic displacements, and changes in the dopant or infiltrating substance, like polymers, are the results of these interactions[8]. In PSi infiltrated with a doped polymer (PEO-based nanocomposites), the refractive index rises as gamma doses increase, indicating structural alterations and increased optical density. This characteristic is very helpful in photonic crystal structures (PhCs) that use PSi as a component layer[10].

Photonic crystals are artificial periodic optical nanostructures that manipulate the propagation of electromagnetic waves by creating photonic bandgaps[11–17]. With novel optical characteristics that are extremely sensitive to radiation exposure, research in photonic structures has created new possibilities for creating gamma dosimeters with improved performance. There are several features and considerations to make while building the best PhCs as radiation dosimeters. The most important property is the material's susceptibility to radiation. It is essential to consider the material's sensitivity to radiation interaction[18–21]. Ref[18]. used 2D- silicon PhCs as gamma densitometry in the visible range and achieved sensitivity 150 nm/RIU. Ref[22]. designed PhC fiber used as radiotherapy dosimeters. According to studies, PSi-based PhCs are very effective radiation dosimeters because gamma radiation can cause alterations in their resonant wavelengths and photonic bandgap[23,24]. This sensitivity results from the PSi layers' structural integrity and accurate modulation of the refractive index, even at different radiation dosages[25]. Ref[8]. investigated a 1D- defective PhC as gamma densitometry and achieved high sensitivity 205 nm/RIU.

Quasi-periodic structures have attracted significant interest in their ability to engineer wave interactions beyond the limits of periodic structures, offering unique properties like fractal bandgaps, localized states, and anomalous dispersion[26–29]. Recent advances in Thue-Morse, Fibonacci, and Rudin-Shapiro structures demonstrate their potential for applications in high-efficiency filters[30–35], and topological photonics[36]. The family of photonic structures known as Thue-Morse quasi-periodic PhCs is distinguished by an aperiodic, randomized layer arrangement. In contrast to periodic or random systems, these structures display unique optical characteristics such as band gaps and localized modes. Thue-Morse PhCs are perfect for use in optical sensing because of their aperiodicity, which increases their sensitivity to outside influences[37]. When materials like PSi and nanocomposites are included in Thue-Morse quasi-periodic PhCs, it becomes possible to develop advanced dosimetry devices with extremely sensitive and adjustable optical responses to gamma radiation[38–40].

In considering everything discussed above, we provide a novel theoretical study of the gamma-ray radiation dosimeter based on different structures of a 1D-quasi periodic-PhC. The structures consisted of aluminum oxide (Al_2O_3) as layer B and PSi infiltrated with PEO nanocomposite as layer A. These structures are five various generalized TMS (GTMS) configurations were examined throughout first, second, and third generations. The aim of studing these structures is to analyze their transmittance behavior and achieve high sensitivity with a high-quality factor for any gamma radiation dose without using defect layer. The proposed study indicate that the 3GTM(2,1) and GTMS(1,2) configurations hold strong potential for advanced radiation dosimetry applications, offering superior sensitivity and quality factors compared to many conventional designs.

Theoretical model and basic equations

The proposed structures are mainly consisting of layer A and layer B. Layer A is PSi with 10% polymer nanocomposite (PEO) inside the pores, and layer B is Al_2O_3. The thicknesses of A and B are 200 nm and 120 nm. PEO is considered the active material for gamma doses.

The following formulas (λ in μm) can be used to compute the RIs of Al_2O_3 according to the Sellmeier equation by fitting the experimental data in Ref[41]., and the PSi containing PEO according to Bruggeman's effective equations[42]:

$$n_{\mathrm{Al2O3}} = -2.012168 + \frac{4.352187\lambda^{2}}{\lambda^{2} - 0.045773^{2}} + \frac{0.117166\lambda^{2}}{\lambda^{2} - 0.187027^{2}} \tag{1}$$

$$\mathrm{n_{PSi}} = 0.5\sqrt{\psi + \sqrt{\psi^{2} + 8\,\mathrm{n_{si}^{2}}\,\mathrm{n_{PEO}^{2}}}},\ \psi = 3\,\mathrm{P}\,\left(\mathrm{n_{PEO}^{2}} - \mathrm{n_{si}^{2}}\right) + \left(2\,\mathrm{n_{si}^{2}} - \mathrm{n_{PEO}^{2}}\right), \tag{2}$$

where P is the volume fraction of PEO in the PSi matrix, and $\mathrm{n_{Si}} = 3.7$. The RI and thermo-optic coefficient of Si is slightly affected with gamma doses up to 1000 kGy and 66.5 kGy (less than 5×10^{-5} and 2.3×10^{-4}), respectively[43]. Ahmed et al.[44] used Monte Carlo codes to study the effect of gamma doses on Si-PhC. They found that dispersion, thermo-optic coefficient, temperature sensitivity, characteristic group index, peak center, and peak width are constant for high doses up to 1 MGy. The optical properties of Al_2O_3 seem to be not changed by changing the gamma doses (even at 46 KGy)[41]. Al_2O_3 can be stabilized with PSi[45–47]. To ensure precise and effective infiltration of polymer nanocomposites into porous silicon (PSi), several proven methods are available based on recent research. These methods vary depending on the pore size, and desired application[48–52].

The RI of PEO can be calculated at different doses of gamma as follows ($300\ \mathrm{nm} \leq \lambda \leq 800\ \mathrm{nm}$, and λ should be in μm in equations)[6]:

At a gamma dose of 0 Gy:

$$n_{\mathrm{PEO}} = -\,50.99\,\lambda^{3} + 109.7\,\lambda^{2} - 78.54\,\lambda + 20.21 \tag{3}$$

At a gamma dose of 100 Gy:

$$n_{\mathrm{PEO}} = 1267.32\,\lambda^{6} - 4530.09\,\lambda^{5} + 6714.24\,\lambda^{4} - 5289.53\,\lambda^{3} + 2341.49\,\lambda^{2} - 554.456\,\lambda + 61.5716 \tag{4}$$

At a gamma dose of 200 Gy:

$$n_{\mathrm{PEO}} = 41.43\,\lambda^{4} - 101.9\,\lambda^{3} + 93.13\,\lambda^{2} - 37.84\,\lambda + 14.15 \tag{5}$$

The transfer matrix method (TMM) is used to calculate the transmittance (T) of normal incident ($\theta = 0$) transverse electric EMWs from the air passing through Thue-Morse Quasi-periodic PhC at different doses of gamma radiation as follows[53–61]:.

$$T\,(\%) = 100 \times \frac{p_s}{p_0} \lfloor t \rfloor^{2} \tag{6}$$

where,

$$t = \frac{2p_0}{\left(A_{11} + A_{12}p_s\right)p_0 + \left(A_{21} + A_{22}p_s\right)} \tag{7}$$

$$\begin{vmatrix} A_{11} & A_{12} \\ A_{21} & A_{22} \end{vmatrix} = \left(a_H a_L\right)^{N}\left(a_L a_H\right)^{N}, \tag{8}$$

$$p_i = n_i\,cos\left(\theta_i\right), \tag{9}$$

where $i = 0$ (for air) , H (for PSi infiltrated with PEO) , L (for Al_2O_3) , and s (for substrate) . The RIs of substrate and air are 1.52 and 1, respectively.

$$a_H = \begin{bmatrix} cos\sigma_H & \left(-\frac{i}{p_H}\right) sin\sigma_H \\ -ip_H\,sin\sigma_H & cos\sigma_H \end{bmatrix}, \tag{10}$$

$$a_L = \begin{bmatrix} cos\sigma_L & \left(-\frac{i}{p_L}\right) sin\sigma_L \\ -ip_L\,sin\sigma_L & cos\sigma_L \end{bmatrix}, \tag{11}$$

$$\sigma_H = \frac{2\pi}{\lambda} d_H n_H cos\theta_H \tag{12}$$

$$\sigma_L = \frac{2\pi}{\lambda} d_L n_L cos\theta_L \tag{13}$$

Results and discussions

Figure 1a plots the refractive index of a PEO against the wavelength of light (300–800 nm) using both experimental data[6] (marked as stars) and the fitted data (continuous lines) mention in Sect. 2 for varying gamma radiation dosages (0 Gy, 100 Gy, and 200 Gy). According to the agreement between experimental and fitted data, the refractive index behavior of the material at various gamma dosages is accurately predicted by the fitted model (created with MATLAB). The refractive index changes with increasing gamma radiation dose (from 0 Gy to 200 Gy), especially at shorter wavelengths. Changes in the molecular alignment of the polymer or structural density are probably the causes of the increase in refractive index with increasing gamma radiation[62]. Exposure to gamma radiation frequently results in cross-linking in polymer nanocomposites, which raises their density and refractive index. This behavior is in line with research on radiation-sensitive polymers and nanocomposites based on PEO[63]. So, this material is suited for optical sensing and dosimetry due to its sensitivity to gamma radiation, as seen by its increased refractive index at 200 Gy compared to 0 Gy.

Figure 1b shows the effect of PSi on the refractive index of the gamma-irradiated material (PEO). For PSi infiltrated with gamma-irradiated material (PEO), the Bruggeman or Maxwell-Garnett theories are frequently used to describe the refractive index as mentioned in Eq. (2). These models take into account the optical characteristics of PEO. The porous structure of PSi and the initial characteristics of the infiltrating PEO are the main factors that govern the refractive index. The refractive index fluctuation is usually more pronounced at shorter wavelengths (300–500 nm) because of larger dispersion effects. Since there is less material dispersion in the longer wavelength range, the refractive index stabilizes as the wavelength increases (beyond 600 nm), thus the impact of gamma radiation may seem less noticeable.

At 0 Gy, the refractive index shows how PSi and unirradiated PEO interact at baseline. Throughout the wavelength range, the values are comparatively constant. In comparison to 0 Gy, the refractive index rises at

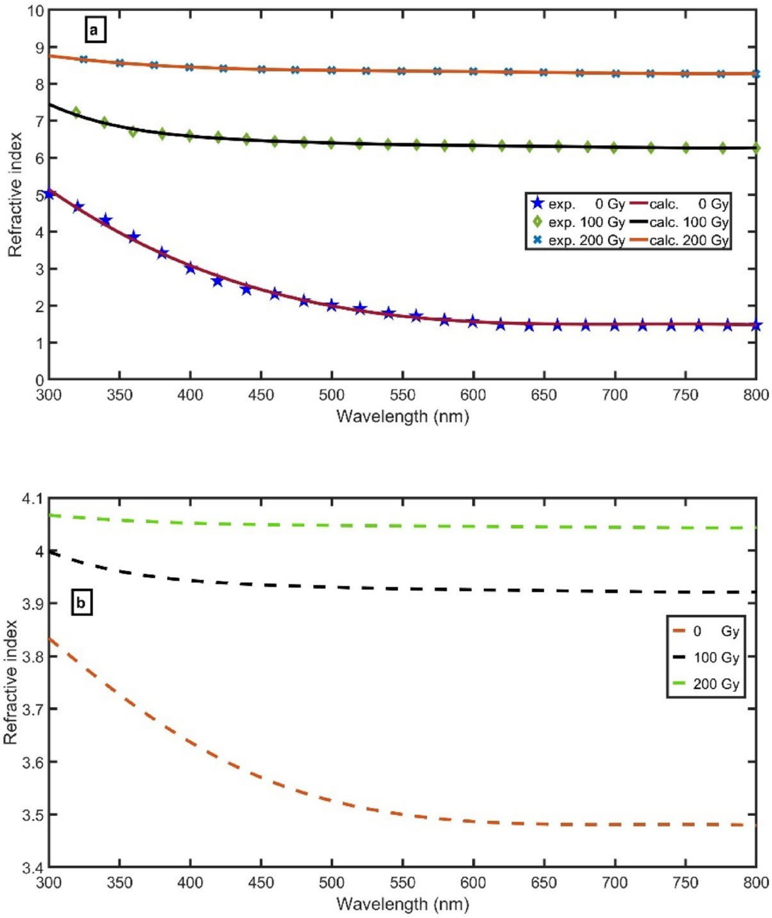

Fig. 1. (**a**) Experimental[6] and fitted refractive index of PEO, and (**B**) refractive indices of PSi infiltrated with PEO at $P = 10\,\%$ at different doses.

100 and 200 Gy, with the effects being more pronounced at shorter wavelengths. The shift indicates gamma radiation-induced structural alterations in PEO. By comparing different doses, the shift demonstrates a dose-dependent rise in refractive index, hence validating the composite material's gamma radiation sensitivity.

PSi containing 10% PEO is used to minimize changes in refractive index under radiation exposure. When pure PEO layers are used, the refractive index increases significantly with radiation, as clearly shown in Fig. 1(a). This causes the photonic bandgap and resonant peaks to shift markedly toward higher wavelengths, moving them outside the relevant experimental range (we can't guess the experimental refractive index outside the range of concern). Additionally, resonant peaks originally located within the bandgap may shift out, while new peaks can appear from the lower-wavelength side—both of which are undesirable for sensing applications. We optimized the ratio of PEO in PSi by getting refractive indices that make all bandgaps (at 0 Gy, 100 Gy, and 200 Gy) inside the wavelength range of concern[6].

The following parts examine the optical properties of GTMS-based quasi-periodic PhCs for a range of generations and configurations. Five constructions are the subject of the study: GTM(1,1), GTM(2,1), GTM(3,1), GTM(1,2), and GTM(1,3). The structural design and associated transmittance spectra of each building are examined at different dosages of gamma radiation (0 Gy, 100 Gy, and 200 Gy). For every configuration, the analysis is separated into two main parts: (1) the PhC construction, which describes the alternating layer arrangement, and the quasi-periodic sequence used, and (2) the transmittance spectra, which shows the evolution of the photonic bandgap and its sensitivity to changes in the refractive index caused by gamma radiation. The optical behavior of these structures is further clarified by the generational analysis (first, second, and third) that shows the effects of growing quasi-periodicity. The goal of this methodical technique is to determine the ideal mix of material layers and quasi-periodic order to produce the most flexible and sensitive PhC design for gamma dosimetry applications.

The recursive relation can be defined as: $S_q = S_{q-1}^{m}\overline{S}_{q-1}^{\,n}$ for $q \geq 1$(integer). For GTMS (*m*=*1*, *n*=1), the initial sequences being $S_0 = A$ and $S_1 = AB$[30,64,65], where *m* and *n* are the successive repetitions of the sequences with *m* = 1 and *n* = 1. For the second sequence, $S_2 = S_1^1\overline{S}_1^{\,1} = 2\mathrm{GTM}\ (1,\ 1) = ABBA$. On the other hand, the third sequence can be represented as $S_3 = S_2^1 \overset{-1}{S_2} = 3\mathrm{GTM}\ (1,\ 1) = ABBABAAB$, etc. For simplicity, each A is converted to AB, and each B is converted to BA.

For GTMS (*2*, *1*), the initial sequences being $S_0 = A$and $S_1 = AAB$. For the second sequence, $S_2 = S_1^1 \overset{-1}{S_1} = 2\mathrm{GTM}\ (2,\ 1) = AABAABBAA$. On the other hand, the third sequence can be represented as $S_3 = S_2^1 \overset{-1}{S_2} = 3\mathrm{GTM}\ (2,\ 1) = AABAABBAABAAAABAAB$, etc. For simplicity, each A is converted to AAB, and each B is converted to BAA.

For GTMS (*3*, *1*), the initial sequences being $S_0 = A$ and $S_1 = AAAB$. For the second sequence, $S_2 = S_1^1 \overset{-1}{S_1} = 2\mathrm{GTM}\ (3,\ 1) =$ AAABAAABAAABBAAA. On the other hand, the third sequence can be represented as $S_3 = S_2^1 \bar{S}_1^2 = 3\mathrm{GTM}\,(3,1) =$ AAABAAABAAABBAAAAAABAAABAAABBAAAAAABAAABAAABBAAABAAAAAAABAAABAAAB, etc. For simplicity, each A is converted to $AAAB$, and each B is converted to $BAAA$. We selected five GTMS configurations to evaluate the impact of increasing quasi-periodicity and dielectric contrast on dosimeter sensitivity and quality. The following study is limited to theoretical modeling, and further experimental validation is required to confirm the observed sensitivity trends under real-world conditions.

GTM(1,1)

The GTMS (1,1) quasi-periodic PhCs for the following four generations: zeroth (0 GTM(1,1)), first (1 GTM(1,1)), second (2 GTM(1,1)), and third (3 GTM(1,1)) are constructed in Fig. 2. The structure is built on alternating layers, A and B, where layer A is PSi infiltrated with PEO, and layer B is made of Al_2O_3. The most basic structure is the zeroth generation (Fig. 2a), which comprises just one layer of material A. The sequence changes according to the recursive Thue-Morse rule, which states that each sequence is created by attaching the complement of the one before it, as the generation order rises. In the first generation (Fig. 2b), for example, layers A and B alternate, whereas in the second generation (Fig. 2c), the structure is extended by repeating the pattern in a quasi-periodic fashion as follows: ABBA. The third generation (Fig. 2d) adds even more complexity, making the layer arrangement more complex (ABBABAAB). One essential feature of Thue-Morse quasi-periodicity is the hierarchical sequence generation, which adds special optical features including numerous photonic band gaps and improved tunability.

Depending on the structural complexity, the photonic bandgap properties are generated by the interaction of low-refractive-index (Al_2O_3) and high refractive-index (PSi + PEO). Quasi-periodic ordering improves light localization and adds special optical characteristics, which makes these PhCs perfect for gamma dosimetry and other applications requiring accurate light manipulation[66].

Figure 3a-c studies the transmittance spectra $1\mathrm{GTM}\,(1{,}1)^4$, $2\mathrm{GTM}\,(1{,}1)^2$ and 3GTMS (1,1) structures under gamma radiation (0 Gy, 100 Gy, and 200 Gy) doses in range (500–800 nm) wavelength. The superscripts (4 and 2) in these structures donate to the repetitions of the GTMS (1,1) unit cell. Figure 3a-c illustrates how the quasi-periodic layer arrangement affects the PhC's optical characteristics with the GTMS (1,1) structures. Interference and creation of a photonic bandgap are caused by changes between refractive-index materials (PSi infiltrated with PEO and Al_2O_3). The high refractive index contrast between PSi infiltrated with PEO and Al_2O_3made them suitable for creating photonic bandgaps. The spectral response of the PhC becomes more complex as the quasi-periodic order increases gradually from one to third generation. In higher generations, the position, width, and quantity of photonic bandgaps are directly influenced by the increased layer thickness and improved structural symmetry. Since the refractive index of PSi and PEO layers is sensitive to radiation exposure, this hierarchical design is especially useful for applications like gamma dosimetry. Therefore, by examining their transmittance spectra, the different optical characteristics of these structures can be used to detect and measure gamma radiation.

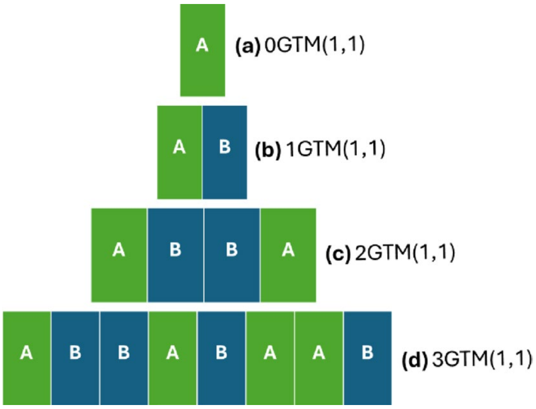

Fig. 2. GTMS (1,1) quasi-periodic PhC using layer A (PSi infiltrated by PEO) and layer B (Al_2O_3) (**a**) zeroth, (**b**) first, (**c**) second, and (**d**) third generations.

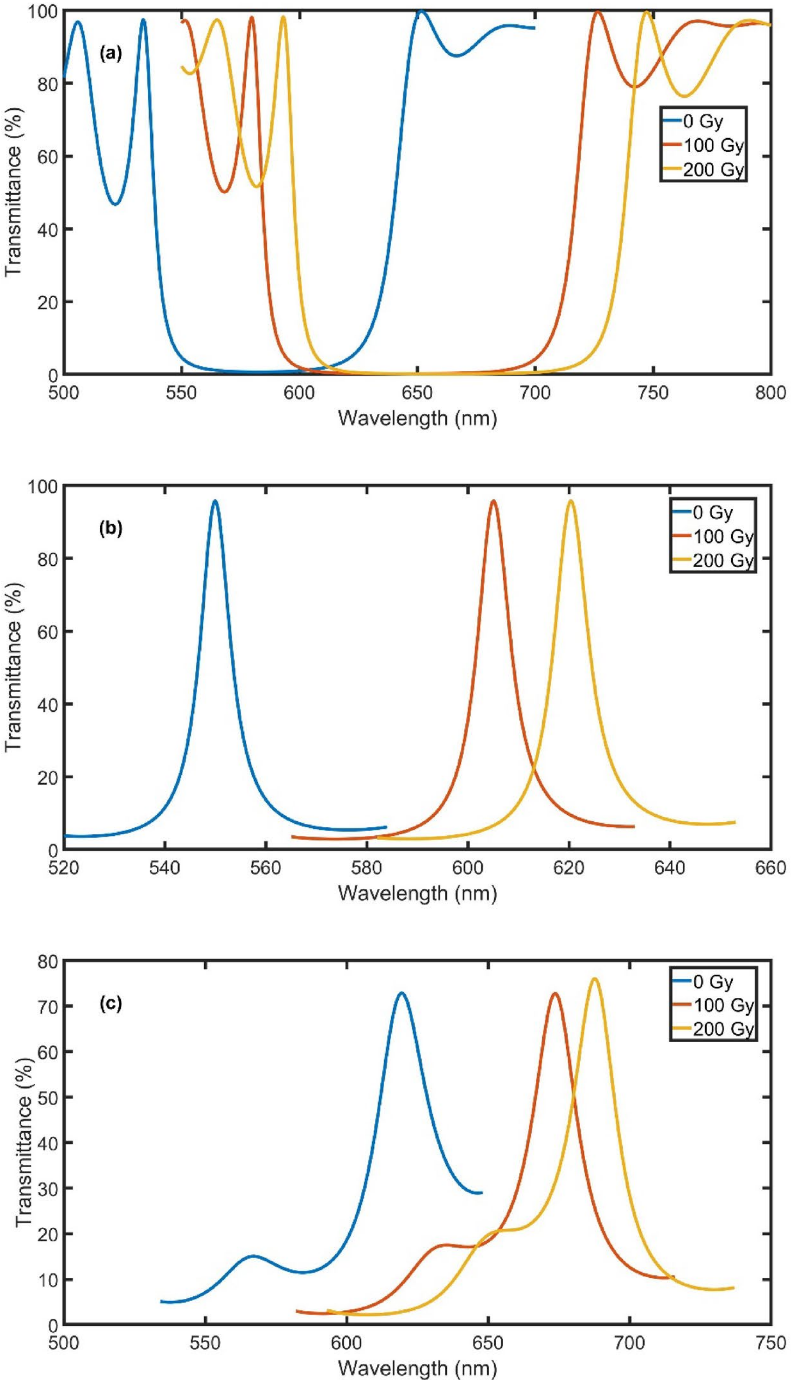

Fig. 3. Transmittance for GTM (1,1) quasi-periodic PhC sequences; (**a**) $1\text{GTM}\,(1{,}1)^4$, (**b**) $2\text{GTM}\,(1{,}1)^2$, and (**c**) 3GTM (1,1), at different gamma doses.

Figure 3a shows the transmittance of the first generation of the GTMS (1,1) structure which is repeated four times. Because there are fewer layers and a simpler structure, the bandgap is comparatively narrow. Due to gamma-induced modifications in the refractive indices of the component materials, a small redshift of the bandgap is seen at 100 Gy. At 200 Gy, the redshift increases, and the bandgap's depth increases, suggesting radiation-induced defects and degeneration in the structural homogeneity. Figure 3b shows the transmittance of the second generation of the GTMS (1,1) structure which is repeated two times. It is noted that the resonance peak appears and is like a defect mode. This behavior reflects the increased structural complexity and sensitivity to changes in refractive index brought on by gamma radiation. With an increase in the gamma dose from 0 Gy to 200 Gy, the resonance peak shifts to higher wavelengths from 549.95 nm to 620.37 nm with a high intensity of approximately (95%), respectively. Figure 3c shows the most intricate transmittance spectra of the third generation of the GTMS (1,1) characterized by the localized defect mode at higher wavelengths compared to the second generation in Fig. 3b. A defect mode appears at 619.42 nm with intensity (72.84%) at 0 Gy gamma irradiation dose. Once, increased to 100 Gy, and 200 Gy, the defect mode appears at 673.61 nm, and 687.68 nm with intensity (72.77%, and 76.04%), respectively.

These data demonstrate that as quasi-periodicity increases, sensitivity to gamma radiation gradually improves. The interaction between material sensitivity and quasi-periodic ordering highlights the promise of PhCs based on GTMS in radiation dosimetry and other optical applications.

GTM(2,1)

In this section, using the two layers of type A (PSi + PEO) and one layer of type B (Al_2O_3) the GTMS (2,1) sequence is built according to the Thue-Morse quasi-periodic rule as shown in Fig. 4a-d. As the most basic building block, the zeroth-generation structure starts with a single (A) layer. The first generation's expansion of the sequence is (AAB). The second generation uses the replacement rule to create (AABAABBAA), and the third generation changes the sequence to (AABAABBAAAABAABBAABAAAABAAB). By altering the refractive index contrast and quasi-periodicity of the system, these designs introduce a distinctive spatial arrangement of dielectric materials that have a major impact on the optical properties.

Compared to GTMS(1,1), this hierarchical structure offers a clear advantage in managing photonic bandgaps. Controlling light propagation depends heavily on the layered configuration of GTMS(2,1) across generations, especially in photonic systems exposed to external influences such as gamma radiation.

Figure 5a–c shows the transmittance spectra of GTMS(2,1) structures for the first, second, and third generations with different repeated unit cells at gamma doses of 0 Gy, 100 Gy, and 200 Gy. Due to their intricate quasi-periodic sequences and light interactions with alternating layer types, these generations exhibit distinct optical properties. Figure 5a presents the transmittance spectra for the first generation, $1\mathrm{GTM}\,(2{,}1)^4$, revealing a single major photonic bandgap between 613.60 nm and 646.08 nm. The $1\mathrm{GTM}\,(2{,}1)^4$ structure shows a major photonic bandgap that broadens and redshifts with increasing gamma doses due to radiation-induced changes in the refractive index of PSi/PEO. Compared to $1\mathrm{GTM}\,(1{,}1)^4$, the bandgap in $1\mathrm{GTM}\,(2{,}1)^4$ occurs at a longer wavelength, changes in the optical properties of the constituent layers.

Figure 5b shows the transmittance of the second generation repeated two times unit cell ($2\mathrm{GTM}\,(2{,}1)^2$). The sequences of this generation are more complicated than the first generation, leading to an increase the interferences. This leads to the formation of the localized defect mode with high intensity and sharpness. By comparing this structure with the before structure $2\mathrm{GTM}\,(1{,}1)^2$, we noticed that the current structure ($2\mathrm{GTM}\,(2{,}1)^2$) gave resonance peak (like defect mode) with high intensity and more sharpener. For the effect of gamma-ray radiation (from 0 Gy to 200 Gy) on the defect mode, the defect mode shifts to a higher wavelength with high intensity. This indicates that gamma radiation enhanced the refractive index of layer A, enhanced the contrast between layer A and dielectric layer B, and reflected in the transmittance spectra of this structure.

Figure 5c shows the transmittance of the third generation 3GTM (2,1). This generation is a highly complicated quasi-structure, leading to stronger interferences and creating highly localized defect modes more sensitive to any dose of gamma-ray radiation. At 0 Gy, the defect mode appears at 516.19 nm with intensity reaching 100%. Once the gamma dose is applied, this defect mode shifts at more distance of wavelengths (Ex; 570.88 nm, and 586.89 nm at 100 Gy, and 200 Gy, respectively. This behavior is based on the higher refractive index of layer A (PSi infiltrated with PEO) increases the strength of the localization and the path length. In addition, the intensity of this defect mode decreases (to 77.55%, and 67.27%) by increasing the gamma-ray doses (100 Gy, and 200 Gy), respectively. As gamma doses increase, the intensity of light transmitted through the defect mode decreases, primarily due to the combined effects of absorption, scattering, and alterations in the refractive index. Besides, increasing the thickness of photonic crystal multilayer films typically reduces transmittance due to enhanced interference, stronger absorption, and more pronounced photonic bandgaps[67–70]. This indicates that this structure is highly sensitive to any optical properties' changes in the structure. Compared to the third-generation structure 3GTM (1,1) discussed in the previous section, the 3GTM (2,1) structure is better suited for use as a gamma dosimeter. This is due to its highly localized defect mode, which exhibits significant sensitivity to variations in gamma-ray radiation doses.

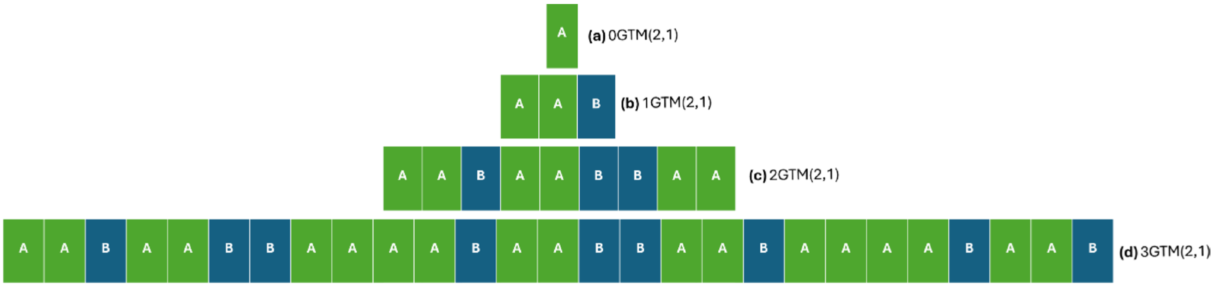

Fig. 4. GTMS (2,1) quasi-periodic PhC using layer A (PSi infiltrated by PEO) and layer B (Al_2O_3) (**a**) zeroth, (**b**) first, (**c**) second, and (**d**) third generations.

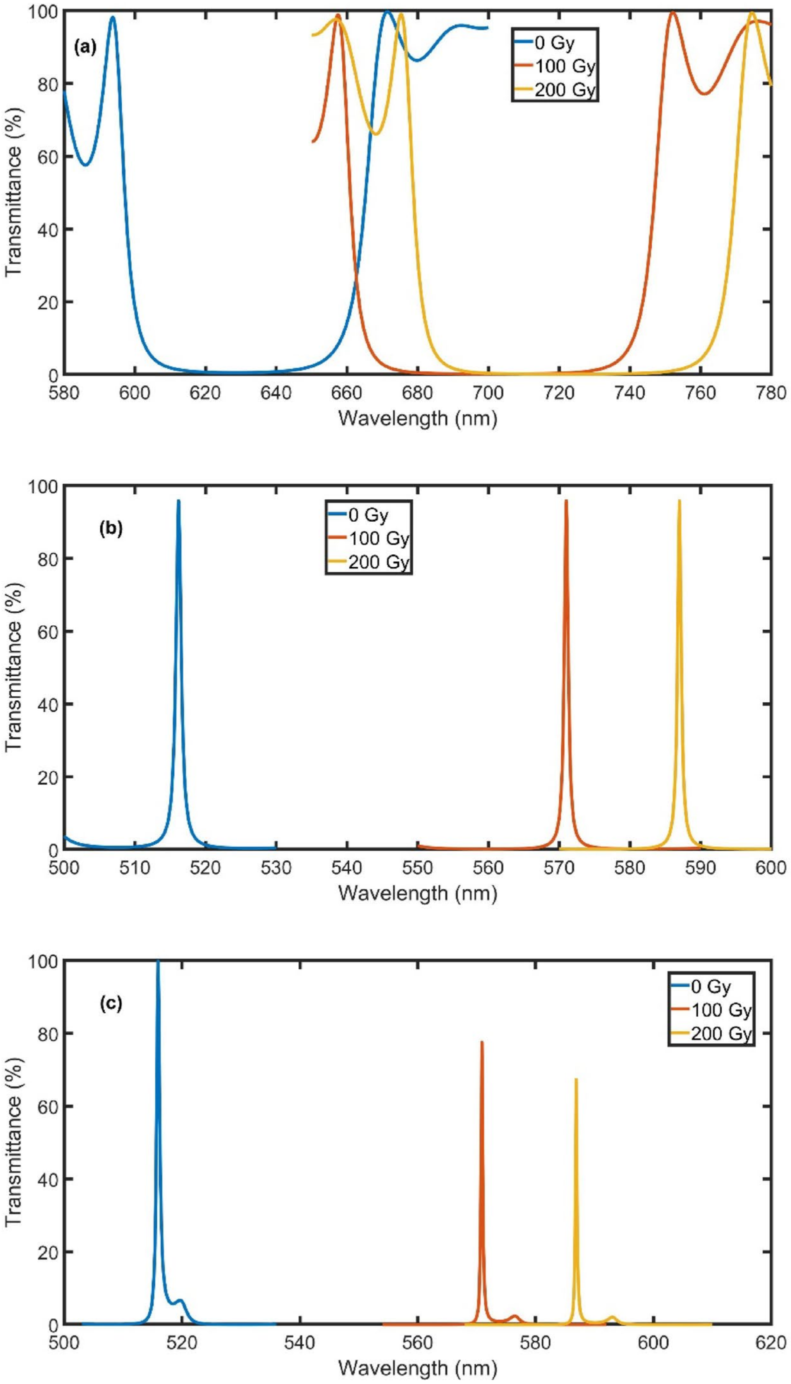

Fig. 5. Transmittance for GTM (2,1) quasi-periodic PhC sequence; (**a**) $1\mathrm{GTM}\,(2{,}1)^{4}$, (**b**) $2\mathrm{GTM}\,(2{,}1)^{2}$, and (**c**) 3GTM (2,1), at different gamma doses.

GTM(3,1)

Figure 6a-d shows the construction of the quasi-periodic GTM(3,1) in the zeroth, first, second, and third generation. The zeroth generation comprises just one layer A. This is the most basic version of the GTMS(3,1) structure, devoid of periodicity and layering. The first generation comprises one B layer after three A layers. The setup is as follows: AAAB. The first-generation structure was repeated to develop the second generation, which had a more intricate arrangement. It comprises several A and B layers arranged as follows: AAABAAABAAABBAAA. By further repeating the second-generation pattern, the third generation is created, which results in an extremely complex layer sequence: (.*AAABAAABAAABBAAAAAAABAABAAABBAAAAAABAAABAAABBAAABAAAAAABAAABAAAB*). This configuration adds a great deal of complexity and strengthens the optical interactions inside the structure.

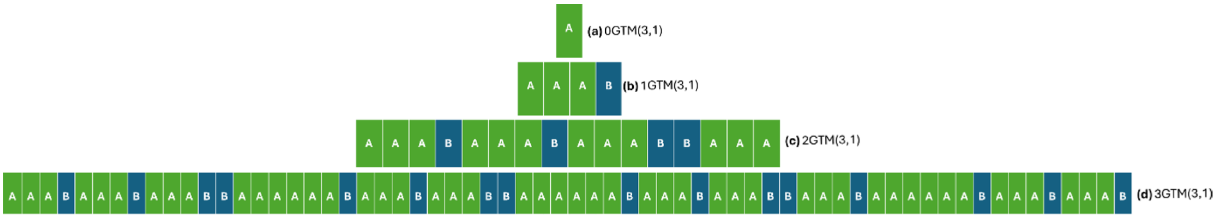

Fig. 6. GTMS (3,1) quasi-periodic sequences using layer A (PSi infiltrated by PEO) and layer B (Al_2O_3) (**a**) zeroth, (**b**) first, (**c**) second, and (**d**) third generations.

Figure 7a-c shows the transmittance spectra of GTMS(3,1) structures are examined for first, second, and third generations with different repeated unit cells at different gamma doses (0 Gy, 100 Gy, and 200 Gy(. Figure 7a shows the transmittance of the first generation of GTMS(3,1) which repeated four times ($1\text{GTM}\,(3{,}1)^4$). This configuration gives a broadened band gap before the effect of gamma-ray radiation (0 Gy). Comparing this structure ($1\text{GTM}\,(3{,}1)^4$) with the first generation of the before structures ($1\text{GTM}\,(1{,}1)^4$) and ($1\text{GTM}\,(2{,}1)^4$), we found that this structure gives a broader band gap at longer wavelengths. The reason behind that is related to the high complexity of this structure and the increase in the number of A layers, which increased the number of interferences and enhanced the optical properties of this structure. Besides, increasing the number of successive layers of A increases the thickness. According to the quarter-wavelength condition ($nd = \lambda/4$)[71], the central wavelength of the band gap (λ) is directly proportional to the thickness of layers.

At 100 Gy, the band gap shifts to lower wavelengths, and at 100 Gy, the band gap shifts again to higher wavelengths but less than the band gap at 0 Gy. This behavior is due to the complexity of this structure.

The transmittance of the second-generation structure, which is repeated two times ($2\text{GTM}\,(3{,}1)^2$), is shown in Fig. 7b. This structure shows a high sharpener band gap and is like (two localized defect modes) at 0 Gy. This band gap gives the same behavior as the ($1\text{GTM}\,(3{,}1)^4$) at 100 Gy and 200 Gy. The transmittance of the third-generation structure (3GTM(3,1)) gives several localized defect modes at each gamma radiation dose, as shown in Fig. 7c. While GTM(3,1) exhibits improved light localization, it is not suited for use as a gamma dosimeter due to its high density of defect modes. When exposed to gamma rays, the structure should show a single, distinct defect mode with a notable intensity shift for gamma dosimetry applications. However, several localized defect modes in GTM(3,1) make it more difficult to analyze gamma-radiation-induced transmittance variations. Because of the numerous modes, it is more difficult to observe changes in position or intensity caused by radiation, which makes this structure less useful for sensing purposes.

GTM(1,2)

In this section, the study depends on the increase of dielectric layers B rather than layer A. Figure 8a-d shows the construction of the GTMS(1,2) in the zeroth, first, second, and third generation. As is known, the zeroth generation is the simplest structure with no periodicity and consists of a single layer A. For the arrangements layer of the first generation will be one layer of A followed by two layers of B (ABB). By applying a quasi-periodic rule to the first-generation structure, the second generation is created. The layers are set up as follows: ABBBBABBA. With more B-layers than A-layers, this structure adds a greater degree of quasi-periodicity. The quasi-periodic arrangement is further extended in the third generation, resulting in a more intricate structure with the layer sequence as follows: ABBBBABBABBABBAABBBBABBAABB. More layers and complex arrangement enhance the creation of photonic bandgaps and interference effects.

In the GTMS(1,2) structures, the proportion of A-layers to B-layers is 2:1. The transmission spectra are considerably impacted by this enhanced B-layer presence in the following ways:

The 1GTM(1,2) structure is repeated four times in this arrangement. As illustrated in Fig. 9a, the transmittance spectra at gamma dosages of 0 Gy, 100 Gy, and 200 Gy indicate a distinct principal photonic bandgap. Because of the higher dielectric homogeneity caused by the greater number of B-layers, the principal photonic bandgap is wider. Gamma-induced changes in the A-layer's refractive index cause the bandgap to slightly redshift at larger doses. Changes in the A-layer refractive index cause redshifts in the bandgap for gamma dosages of 0 Gy, 100 Gy, and 200 Gy. Nevertheless, these shifts are not as noticeable as in structures with fewer B-layers. Comparing between the structures $1\text{GTM}\,(1{,}2)^4$, and $1\text{GTM}\,(2{,}1)^4$, Wider bandgaps that are less sensitive to small variations in refractive index are the result of the increased B-layers, which also improve transmittance stability across the bandgap. For $1\text{GTM}\,(2{,}1)^4$, the increased number of layers A enhanced the refractive index contract and the structure more sensitive to gamma-ray radiation. Wider photonic bandgaps that are less sensitive to small variations in refractive index are the result of the increased B-layers, which also improve transmittance stability across the bandgap.

Figure 9b, shows the transmittance spectra of $2\text{GTM}\,(1{,}2)^2$ which repeated two times in this arrangement. This structure produces clear, easily monitored localized fault modes, which are essential for gamma sensing. Changes in the A-layer refractive index cause redshifts in the defect modes for gamma dosages of 0 Gy, 100 Gy, and 200 Gy. Nevertheless, these shifts are not as noticeable as in systems with fewer B-layers. If we compare this structure with $2\text{GTM}\,(1{,}2)^2$ with $2\text{GTM}\,(2{,}1)^2$, the defect modes are sharper and more sensitive to gamma-ray radiation in $2\text{GTM}\,(2{,}1)^2$.

Without repetition, the third-generation structure is depicted in Fig. 9c, which displays transmittance spectra with a low-intensity (65.61%) localized defect mode at 0 Gy. The structural changes induced by gamma radiation

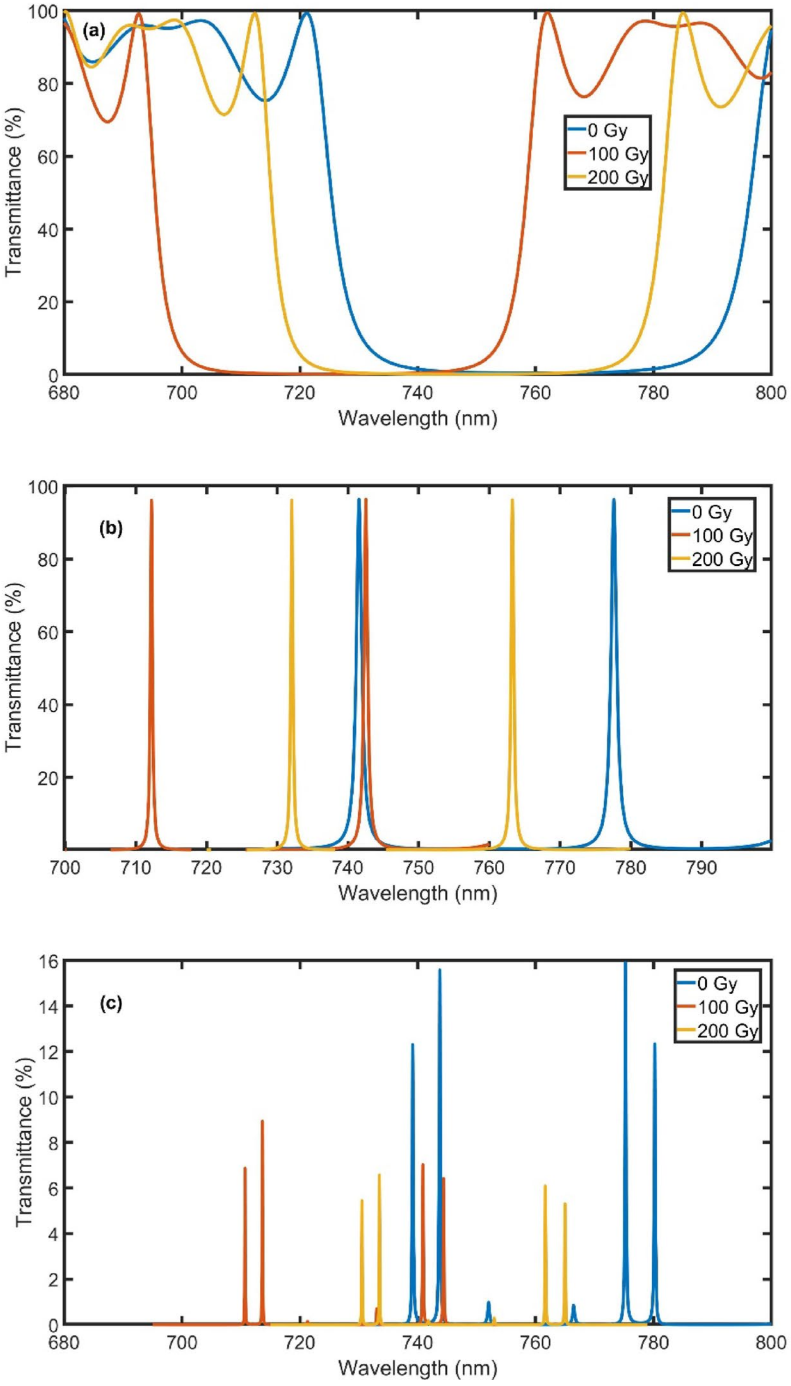

Fig. 7. Transmittance for GTM(3,1) quasi-periodic PhC sequence; (a) $1\mathrm{GTM}\ (3{,}1)^4$, (b) $2\mathrm{GTM}\ (3{,}1)^2$, and (c) 3GTM(3,1), at different gamma doses.

are reflected in the defect modes' shift to longer wavelengths and increase in intensity to (88.18%, and 95.36%) when the gamma dose rises to 100 Gy and 200 Gy, respectively.

GTM (1,3)

As in all sections before, we analyze new structure from quasi-periodic (GTM(1,3)) in which the ratio of layers (1 A:3B). Figure 10a-d shows the construction of this structure in the zeroth, first, second, and third generation. The first generation presents a simple quasi-periodic sequence with three B-layers after one A-layer: ABBB. By repeating the first-generation pattern into a more intricate sequence, the second generation expands the structure: ABBBBBBABBBABBBA. This configuration results in more interfaces and a significant dielectric contrast by increasing the dominance of B-layers. The third generation builds on the second-generation sequence, generating a highly complex structure with many more layers:

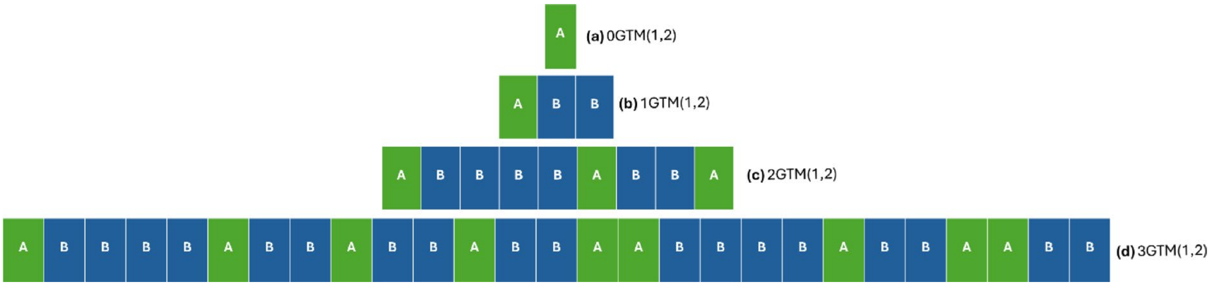

Fig. 8. GTMS(1,2) quasi-periodic sequences using layer A (PSi infiltrated by PEO) and layer B (Al_2O_3) (**a**) zeroth, (**b**) first, (**c**) second, and (**d**) third generations.

ABBBBBBABBBABBBABBBABBBABBBABBBAABBBBBBABBBABBBAABBBBBBABBBABBBAABBB. This complex arrangement results in a highly varied photonic response by increasing the number of contacts and enhancing interference effects.

The transmittance spectra of the first generation which was repeated four times at 0 Gy, 100 Gy, and 200 Gy shown in Fig. 11a-c. At 0 Gy, the band gap with very low width and less intensity appears in Fig. 11a. The reason behind this behavior is the lower number of layers A compared to the increased number of layers B. At higher doses (100 Gy, and 200 Gy) the refractive index of layers A increased and led to an increase in the width of the band gap and shifted to higher wavelengths. In the second generation which was repeated two times, the defect mode appeared with high intensity (95.50%) at a wavelength (606.75 nm) at 0 Gy, as shown in Fig. 11b. By increasing the gamma dose to 100 Gy and 200 Gy, the defect mode shifts to higher wavelengths (647.10 nm, and 659.79 nm) and becomes a sharpener with stability in the intensity (≈ 95%). The single generation 3GTM(1,3) structure exhibits complicated transmittance spectra due to multiple interferences between large numbers of layers. As shown in Fig. 11c, the defect mode appears at wavelength (511.41 nm) with low intensity (39.68%). The defect mode shifts toward longer wavelengths and highly decreases in intensity (14.80%, and 5.38%) when the gamma dose increases to 100 Gy and 200 Gy because of changes in the refractive index and scattering effects.

In conclusion from this section, increases in layer B relative to layer A led to a decrease in the refractive index contrast between the two layers, which broadens the band gap, small red shift to a higher wavelength, and lowers the intensity of the defect modes.

Sensitivity and quality factor (Q-factor) are two important factors used to assess the performance of quasi-periodic PhCs for gamma dosimetry. Sensitivity, which measures how well the structure senses changes in refractive index caused by radiation, is defined as the shift in defect mode wavelength (Δλ) per unit gamma dose. The Q-factor, which is defined as $Q = \lambda/FWHM$, where λ is the resonant wavelength and FWHM is the full-width at half-maximum of the defect mode, indicates how well-localized a defect mode is. The sensitivity and Q-factor of the many different structures show distinct variations in the second and third generations in the two ranges of gamma doses (0–100 Gy, and 100–200 Gy) as shown in Table 1. Sensitivity and Q-factor are exchanged off in the study of various structures. The structures with high Q-values typically have lesser sensitivity.

Out of all the structures that were examined, $2\mathrm{GTM}\,(2{,}1)^2$and 3GTM(2,1) had remarkably high Q-factors (892.2 and 1715.9, respectively) and a moderate sensitivity of 0.55 nm/Gy. Sharp and well-localized defect modes are indicated by these high Q-values, which are advantageous for accurate wavelength identification. Nevertheless, structures from GTMS(1,3), especially 3GTM(1,3), have the highest Q-factor (1929), but their poor defect mode response to radiation results in a relatively low sensitivity of 0.15 nm/Gy, making them less appropriate for gamma sensing.

However, the GTMS(1,2) structures, especially $2\mathrm{GTM}\,(1{,}2)^2$, provide a better-balanced performance with an appropriately high Q-factor of 473 and S = 0.5 nm/Gy. In comparison to higher-order structures, this equilibrium maintains better sensitivity while maintaining effectively acute defect modes. In comparison, 3GTM(1,2) shows a considerable performance trade-off with a lower Q-factor (414.8) and a little lower sensitivity (0.49 nm/Gy).

All things considered, $3\mathrm{GTM}\,(2{,}1)$, and 2GTM(1,2) are the best-performing structures for gamma dosimetry because they offer the best sensitivity and Q-factor balance, ensuring significant and apparent changes in the defect mode while preserving sufficient sharpness for accurate dose measurements.

Structures with too low Q-value, such 3GTM(1,1) (Q = 33.8), lack spectral resolution for accurate detection, whereas structures with too high a Q-value, like 3GTM(1,3), are less useful because of their low sensitivity. Consequently, the best option for gamma dosimetry applications are $3\mathrm{GTM}\,(2{,}1)$, and $2\mathrm{GTM}\,(1{,}2)^2$.

As indicated in Table (2), the performance of the proposed GTMS-based quasi-periodic PhCs as gamma dosimeters is compared with previously published structures in the field of research. In contrast, our $3\mathrm{GTM}\,(2{,}1)$, and GTMS(1,2)-based structures maintain great sensitivity and flexibility under gamma irradiation while offering more stable and well-defined defect modes. These findings demonstrate that the $3\mathrm{GTM}\,(2{,}1)$, and GTMS(1,2) configuration are promising candidates for advanced radiation dosimetry applications since they perform better in terms of sensitivity and quality factors than many traditional designs.

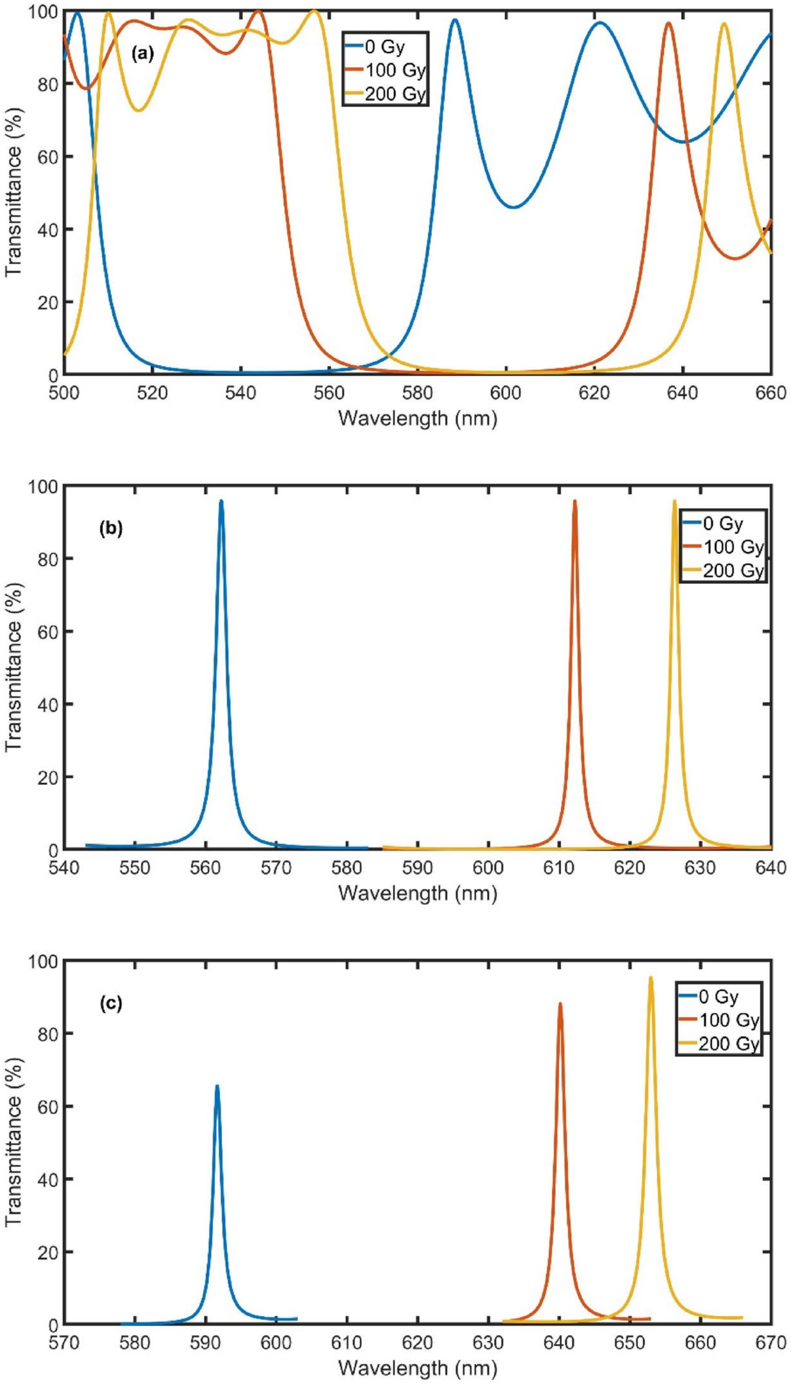

Fig. 9. Transmittance for GTM(1,2) quasi-periodic PhC sequence; (**a**) $1\mathrm{GTM}\ (1{,}2)^{4}$, (**b**) $2\mathrm{GTM}\ (1{,}2)^{2}$, and (**c**) 3GTM (1,2), at different gamma doses.

Conclusion

In this study, we evaluated the viability of many quasi-periodic PhC structures depending on the GTMS as gamma dosimeters by designing and analyzing them. To verify the optical response of the structures, fitting equations for experimental data were included in the theoretical calculations based on the transfer matrix method. A thorough evaluation of the impact of structural complexities on radiation sensitivity, defect mode creation, and transmittance spectra has been performed. The structures were made of aluminum oxide as layer B and PSi injected by PEO nanocomposite as layer A. The best configurations for gamma dosimetry among the configurations under study were 3GTM(2,1) and $2\mathrm{GTM}\ (1{,}2)^{2}$. With a sensitivity of 0.55 nm/Gy and a quality factor of 1715.9, 3GTM(2,1) showed remarkably strong defect mode localization, which qualifies it for extremely sensitive detection. With a sensitivity of 0.5 nm/Gy and a quality factor of 473, $2\mathrm{GTM}\ (1{,}2)^{2}$demonstrated

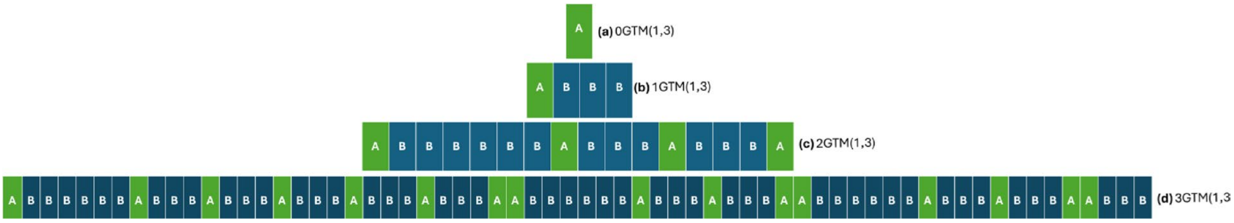

Fig. 10. GTMS(1,3) quasi-periodic sequences using layer A (PSi infiltrated by PEO) and layer B (Al_2O_3) (**a**) zeroth, (**b**) first, (**c**) second, and (**d**) third generations.

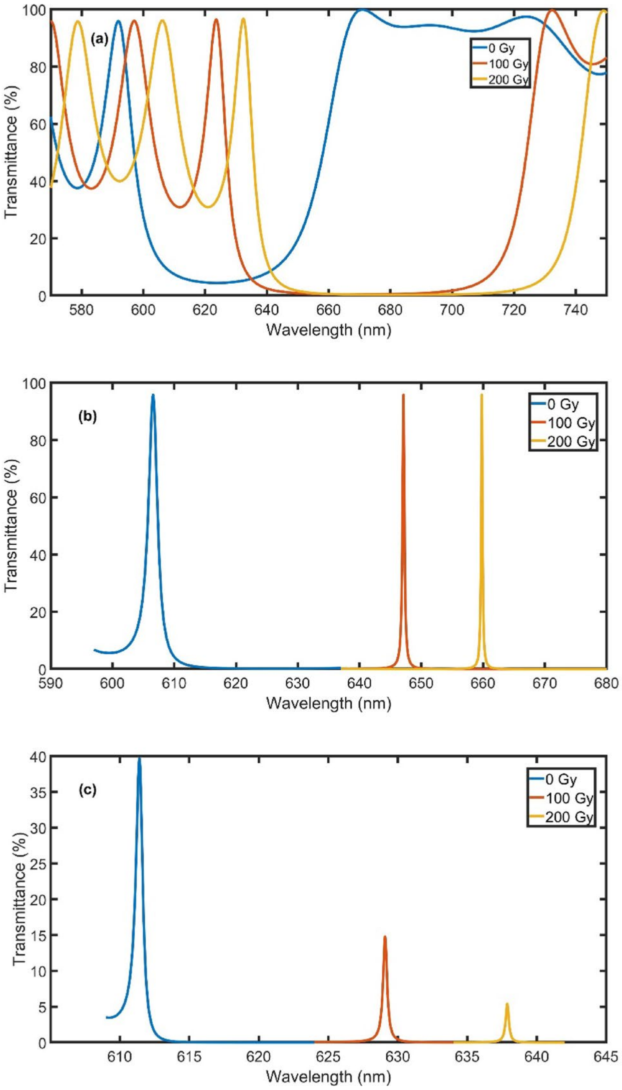

Fig. 11. Transmittance for GTM(1,3) quasi-periodic PhC sequence; (**a**) $1\text{GTM}\,(1{,}3)^4$, (**b**) $2\text{GTM}\,(1{,}3)^2$, and (**c**) 3GTM(1,3), at different gamma doses.

a well-balanced performance that makes it extremely useful for gamma-sensing applications. The suggested designs offer better sensitivity, tunability, and defect mode stability than traditional dosimeters described in the comparsion. Future studies will concentrate on investigating substitute materials with distinct optical characteristics and examining more quasi-periodic structures to boost sensitivity and enhance the tunability of defect modes in order to better optimize the performance of GTMS-based PhCs. The goal of these efforts is to improve theoretical models and find setups that optimize photonic structures' gamma radiation sensitivity.

structure	Gamma range	S (nm/Gy)	Q
2GTM $(1,1)^2$	0–100 Gy	0.55	77.4
	100–200 Gy	0.15	76.6
3GTM (1,1)	0–100 Gy	0.55	33.8
	100–200 Gy	0.14	34.6
2GTM $(2,1)^2$	0–100 Gy	0.55	892.2
	100–200 Gy	0.16	957.4
3GTM (2,1)	0–100 Gy	0.55	1715.9
	100–200 Gy	0.16	1951.8
2GTM $(1,2)^2$	0–100 Gy	0.50	473.0
	100–200 Gy	0.14	467.9
3GTM (1,2)	0–100 Gy	0.49	414.8
	100–200 Gy	0.13	365.5
2GTM $(1,3)^2$	0–100 Gy	0.41	1805.6
	100–200 Gy	0.13	2620.3
3GTM (1,3)	0–100 Gy	0.18	1929.3
	100–200 Gy	0.09	2363.4

Table 1. Sensitivity, and quality factor of the different quasi-periodic phcs.

Ref.	S (nm/Gy)	Q	Range	Structure
2020[72],	0.0013	NC	500 Gy	Fiber grating
2013[73],	0.0002	NC	0–300 Gy	Indigo dye samples
2012[74],	0.00018	NC	6000–65,000	Fiber grating
2018[75],	0.0012	NC	0–500 Gy	Fiber grating
2024[25],	0.265	12,701	0–70 Gy	1D-PhC
2021[18],	0.298	808	0–70 Gy	2D-PhC
Our study 3GTM(2,1)	**0.55**	**1715.9**	**0–100 Gy**	**Thue-Morse Quasi-periodic PhCs**
Our study 2GTM $(1,2)^2$	**0.50**	**473.0**	**0–100 Gy**	**Thue-Morse Quasi-periodic PhCs**

Table 2. Evaluation of different gamma sensors:.

Data availability

The datasets used and/or analysed during the current study available from the corresponding author)Z. A. Zaky(on reasonable request.

Received: 7 February 2025; Accepted: 16 May 2025
Published online: 27 May 2025

References

1. El-Shemy, S. et al. Radiation sensor based on a 1D-periodic structure infiltrated by (B-co-MP) a conjugated copolymer. *Sci. Rep.* **14**, 19829. https://doi.org/10.1038/s41598-024-65312-w (Aug 27 2024).
2. Chmielewski, A., Chmielewska, D., Michalik, J. & Sampa, M. Prospects and challenges in application of gamma, electron and ion beams in processing of nanomaterials. *Nucl. Instrum. Methods Phys. Res., Sect. B.* **265**, 339–346 (2007).
3. Chmielewska, D. Radiation methods and uses in nanotechnology. *Appl. Ionizing Radiation Mater. Process.* **1**, 395–414 (2017).
4. Aziz, S. B. et al. Effect of ohmic-drop on electrochemical performance of EDLC fabricated from PVA: dextran: NH4I based polymer blend electrolytes. *J. Mater. Res. Technol.* **9**, 3734–3745. https://doi.org/10.1016/j.jmrt.2020.01.110 (2020).
5. Mohan, V., Bhargav, P., Raja, V., Sharma, A. & Narasimha Rao, V. Optical and electrical properties of pure and doped PEO polymer electrolyte films. *Soft Mater.* **5**, 33–46 (2007).
6. Qwasmeh, A. A. H. et al. Effects of gamma irradiation on optical properties of Poly (ethylene oxide) thin films doped with potassium iodide. *J. Compos. Sci.* **7**, 194. https://doi.org/10.3390/jcs7050194 (2023).
7. Vaijapurkar, S., Senwar, K. R., Hooda, J. & Parihar, A. The performance evaluation of gamma-and neutron-sensitive superheated emulsion (bubble) detectors. *Radiat. Prot. Dosimetry*. **130**, 285–290. https://doi.org/10.1093/rpd/ncn058 (2008).
8. Sayed, F. A., Elsayed, H. A., Mehaney, A., Eissa, M. & Aly, A. H. A doped-polymer based porous silicon photonic crystal sensor for the detection of gamma-ray radiation. *RSC Adv.* **13**, 3123–3138. https://doi.org/10.1039/D2RA07637C (2023).
9. Levitsky, I. A. Porous silicon structures as optical gas sensors, *Sensors*, vol. 15, pp. 19968–19991, (2015).
10. Nocerino, V., Rea, I., Siciliano, G., De Stefano, L. & Primiceri, E. Polymers modified porous silicon optical (bio) sensors. *TrAC Trends Anal. Chem.* **177**, 117811 (2024).
11. Saini, J., Kumar, A. & Goyal, A. K. Performance Analysis of Chirped Graded Photonic Crystal Resonator for Biosensing Applications, in *Photonics*, p. 1173. (2024). https://doi.org/10.3390/photonics11121173
12. Goyal, A. K., Dash, D., Saini, J. & Massoud, Y. Theoretical analysis of graded-index topological resonator for improved sensing performance. *Opt. Express*. **32**, 4102–4110. https://doi.org/10.1364/OE.511412 (2024).

13. Goyal, A. K., Divyanshu, D. & Massoud, Y. Excitation of optical Tamm state for photonic spin hall enhancement. *Sci. Rep.* **14**, 175. https://doi.org/10.1038/s41598-023-50067-7 (2024).
14. Goyal, A. K., Kumar, A. & Massoud, Y. Performance analysis of heterostructure-based topological nanophotonic sensor. *Sci. Rep.* **13**, 19415. https://doi.org/10.1038/s41598-023-46784-8 (2023).
15. Goyal, A. K., Saini, J. & Massoud, Y. Performance analysis of organic material assisted dynamically tunable excitation of optical Tamm state. *Opt. Quant. Electron.* **55**, 563. https://doi.org/10.1007/s11082-023-04843-4 (2023).
16. Dash, D., Saini, J., Goyal, A. K. & Massoud, Y. Exponentially index modulated nanophotonic resonator for high-performance sensing applications. *Sci. Rep.* **13**, 1431. https://doi.org/10.1038/s41598-023-28235-6 (2023).
17. Goyal, A. K., Kumar, A. & Massoud, Y. Performance analysis of DAST material-assisted photonic-crystal-based electrical tunable optical filter, *Crystals*, vol. 12, p. 992, (2022). https://doi.org/10.3390/cryst12070992
18. Ibrahim, M. S. S., Hamed, M. K. G., El-Okr, M. M., Obayya, S. & Hameed, M. F. O. Highly sensitive photonic crystal gamma ray dosimeter. *Opt. Quant. Electron.* **53**, 348. https://doi.org/10.1007/s11082-021-02968-y (2021).
19. Wang, Z. et al. Color-phase readout radiochromic photonic crystal dosimeter. *Matter* **5**, 4060–4075 (2022).
20. Wang, Z. et al. A high-resolution 3D radiochromic hydrogel photonic crystal dosimeter for clinical radiotherapy. *Mater. Horiz.* **12**, 1234–1245 (2025).
21. Elsaket, A. I., Rashed, A. N. Z., Mohamed, A. E. N. A., Ahmed, H. E. & Zaky, M. M. Highly sensitive gamma ray dosimeter based on dual-core photonic crystal fiber, *Journal of Instrumentation*, vol. 19, p. P02002, (2024).
22. Begum, M. et al. Photonic crystal fibre as a potential medium for radiotherapy dosimetry. *Appl. Radiat. Isot.* **174**, 109771 (2021).
23. Mehaney, A., Abadla, M. M. & Elsayed, H. A. 1D porous silicon photonic crystals comprising Tamm/Fano resonance as high performing optical sensors. *J. Mol. Liq.* **322**, 114978. https://doi.org/10.1016/j.molliq.2020.114978 (2021).
24. Lujan-Cabrera, I. A., Isaza, C., Anaya-Rivera, E. K. & Ramirez-Gutierrez, C. F. Inverse design of incommensurate one-dimensional porous silicon photonic crystals using 2D-convolutional mixture density neural networks. *Photonics Nanostructures-Fundamentals Appl.* **59**, 101260 (2024).
25. Zaky, Z. A., Al-Dossari, M., Hendy, A. S., Zayed, M. & Aly, A. H. Gamma radiation detector using cantor quasi-periodic photonic crystal based on porous silicon doped with polymer. *Int. J. Mod. Phys. B* **38**(30), 2450409 (2024).
26. Dai, C. et al. A proteomics sample metadata representation for multiomics integration and big data analysis. *Nat. Commun.* **12**, 5854. https://doi.org/10.1038/s41467-021-26111-3 (2021).
27. Yu, C., Liu, Y., Zhang, K. & Feng, S. High-sensitivity refractive index sensor based on defective modes of an 8-fold quasi-periodic photonic crystal. *Opt. Commun.* **550**, 129994. https://doi.org/10.1016/j.optcom.2023.129994 (2024).
28. Yang, K. et al. „, *Observation of Thouless pumping of light in quasiperiodic photonic crystals, Proceedings of the National Academy of Sciences, vol. 121, p. e2411793121.* https://doi.org/10.1073/pnas.2411793121 (2024).
29. Zaky, Z. A., Al-Dossari, M., Matar, Z. & Aly, A. H. Effect of geometrical and physical properties of cantor structure for gas sensing applications. *Synth. Met.* **291**, 117167. https://doi.org/10.1016/j.synthmet.2022.117167 (2022).
30. Ali, N. B. et al. Tunable multi-band-stop filters using generalized fibonacci photonic crystals for optical communication applications, *Mathematics*, vol. 10, p. 1240, (2022). https://doi.org/10.3390/math10081240
31. Trabelsi, Y., Ali, N. B. & Kanzari, M. Tunable narrowband optical filters using superconductor/dielectric generalized Thue-Morse photonic crystals. *Microelectron. Eng.* **213**, 41–46. https://doi.org/10.1016/j.mee.2019.04.016 (2019).
32. Ali, N. B. & Kanzari, M. Designing of stop band filters using hybrid periodic/quasi-periodic one-dimensional photonic crystals in microwave domain. *Phys. Status Solidi (a).* **208**, 161–171. https://doi.org/10.1002/pssa.200925531 (2010).
33. Ilyas Antraoui, A. K., Sallah, M. & Zaky, Z. A. Localized modes and acoustic band gaps using different quasi-periodic structures based on closed and open resonators. *Sci. Rep.* **15**, 7633. https://doi.org/10.1038/s41598-025-90691-z (2025).
34. Yue, C., Tan, W. & Liu, J. Photonic band gap properties of one-dimensional Thue-Morse all-dielectric photonic quasicrystal. *Superlattices Microstruct.* **117**, 252–259. https://doi.org/10.1016/j.spmi.2018.03.023 (2018).
35. Segovia-Chaves, F., Vinck-Posada, H. & Gómez, E. A. Transmittance spectrum in a semiconductor-superconductor quasi-periodic Thue-Morse one-dimensional photonic crystal. *Physica C (Amsterdam, Neth.).* **579**, 1353768. https://doi.org/10.1016/j.physc.2020.1353768 (2020).
36. Bandres, M. A., Rechtsman, M. C. & Segev, M. Topological photonic quasicrystals: fractal topological spectrum and protected transport. *Phys. Rev. X.* **6**, 011016. https://doi.org/10.1103/PhysRevX.6.011016 (2016).
37. Xu, H. et al. Optical bistability of graphene in PT – symmetric Thue–Morse photonic crystals. *J. Mater. Sci.* **57**, 6524–6535. https://doi.org/10.1007/s10853-022-07038-6 (2022).
38. De Medeiros, F., Albuquerque, E., Vasconcelos, M. & Mauriz, P. Thermal radiation in quasiperiodic photonic crystals with negative refractive index. *J. Phys.: Condens. Matter.* **19**, 496212 (2007).
39. Agarwal, V., Soto-Urueta, J., Becerra, D. & Mora-Ramos, M. E. Light propagation in polytype Thue–Morse structures made of porous silicon. *Photonics Nanostructures-Fundamentals Appl.* **3**, 155–161 (2005).
40. Zaky, Z. A., Al-Dossari, M., Hendy, A. S., Zayed, M. & Aly, A. H. Gamma radiation detector using cantor quasi-periodic photonic crystal based on porous silicon doped with polymer. *Int. J. Mod. Phys. B.* **38**, 2450409. https://doi.org/10.1142/s0217979224504095 (2024).
41. Esposito, F. et al. Optical properties of thin films monitored in real-time at high gamma radiation doses using long period fiber gratings. *Opt. Laser Technol.* **176**, 111019. https://doi.org/10.1016/j.optlastec.2024.111019 (2024).
42. Zaky, Z. A., Alamri, S., Zhaketov, V. & Aly, A. H. Refractive index sensor with magnified resonant signal. *Sci. Rep.* **12**, 13777. https://doi.org/10.1038/s41598-022-17676-0 (2022).
43. El-Shemy, S. et al. Radiation sensor based on a 1D-periodic structure infiltrated by (B-co-MP) a conjugated copolymer. *Sci. Rep.* **14**, 19829. https://doi.org/10.1038/s41598-024-65312-w (2024).
44. Ahmed, Z. et al. Assessing radiation hardness of silicon photonic sensors. *Sci. Rep.* **8**, 13007. https://doi.org/10.1038/s41598-018-31286-9 (2018).
45. Min-Dianey, K. A. et al. Near-infrared transmissive properties of porous Si/Al2O3 photonic crystal band gaps. *Mater. Today Commun.* **33**, 104323. https://doi.org/10.1016/j.mtcomm.2022.104323 (2022).
46. Seredin, P. et al. Ultrathin nano-sized Al2O3 strips on the surface of por-Si. *Mater. Sci. Semiconduct. Process.* **39**, 551–558. https://doi.org/10.1016/j.mssp.2015.05.067 (2015).
47. Peng, S. et al. Three-dimensional single gyroid photonic crystals with a mid-infrared bandgap. *Acs Photonics.* **3**, 1131–1137. https://doi.org/10.1021/acsphotonics.6b00293 (2016).
48. Harraz, F. & Salem, A. Electrosynthesis of Intrinsically Conducting Polymers/Silicon Nanocomposites: Formation Mechanism and Optical Properties, Vol. 1. 632–635 (2012).
49. Harraz, F. A. & Salem, A. M. Enhancement of porous silicon photoluminescence by chemical and electrochemical infiltration of conducting polymers. *Scripta Mater.* **68**, 683–686. https://doi.org/10.1016/j.scriptamat.2013.01.021 (2013).
50. Shahbazi, M. A. et al. Poly (methyl vinyl ether-alt-maleic acid)-functionalized porous silicon nanoparticles for enhanced stability and cellular internalization. *Macromol. Rapid Commun.* **35**, 624–629. https://doi.org/10.1002/marc.201300868 (2014).
51. Lopez, H. A., Chen, X. L., Jenekhe, S. A. & Fauchet, P. M. Tunability of the photoluminescence in porous silicon due to different polymer dielectric environments. *J. Lumin.* **80**, 115–118. https://doi.org/10.1016/S0022-2313(98)00078-7 (1998).
52. Marsal, L. et al. Polymer microfibers obtained using porous silicon templates. *Phys. Status Solidi (a).* **205**, 2437–2440. https://doi.org/10.1002/pssa.200723556 (2008).
53. Yeh, P. *Optical Waves in Layered Media* (Wiley New York, 1988).

54. Zaky, Z. A., Al-Dossari, M., Hendy, A. S., Badawy, W. M. & Aly, A. H. Periodic open and closed resonators as a biosensor using two computational methods. *Sci. Rep.* **14**, 11943. https://doi.org/10.1038/s41598-024-61987-3 (2024).
55. Zaky, Z. A. et al. Theoretical analysis of porous silicon one-dimensional photonic crystal doped with magnetized cold plasma for hazardous gases sensing applications. *Opt. Quant. Electron.* **55**, 584. https://doi.org/10.1007/s11082-023-04907-5 (2023).
56. Zaky, Z. A. et al. Theoretical optimization of Tamm plasmon polariton structure for pressure sensing applications. *Opt. Quant. Electron.* **55**, 738. https://doi.org/10.1007/s11082-023-05023-0 (2023).
57. Ameen, A. A., Al-Dossari, M., Zaky, Z. A. & Aly, A. H. Studying the effect of quantum Dots and parity-time symmetry on the magnification of topological edge state peak as a pressure sensor. *Synth. Met.* **292**, 117233. https://doi.org/10.1016/j.synthmet.2022.117233 (2023).
58. Al-Dossari, M., Zaky, Z. A., Awasthi, S. K., Amer, H. A. & Aly, A. H. Detection of glucose concentrations in urine based on coupling of Tamm–Fano resonance in photonic crystals. *Opt. Quant. Electron.* **55**, 484. https://doi.org/10.1007/s11082-023-04621-2 (2023).
59. Zaky, Z. A., Al-Dossari, M., Sharma, A. & Aly, A. H. Effective pressure sensor using the parity-time symmetric photonic crystal. *Phys. Scr.* **98**, 035522. https://doi.org/10.1088/1402-4896/acbcae (2023).
60. Tammam, M. T. et al. Defected Photonic Crystal Array Using Porous GaN as Malaria Sensor, presented at the IOP Conference Series: Materials Science and Engineering, (2021). https://doi.org/10.1088/1757-899X/1171/1/012005
61. Zaky, Z. A. et al. Photonic crystal with magnified resonant peak for biosensing applications. *Phys. Scr.* **98**, 055108. https://doi.org/10.1088/1402-4896/accbf1 (2023).
62. De Deene, Y. Radiation dosimetry by use of radiosensitive hydrogels and polymers: mechanisms, state-of-the-art and perspective from 3D to 4D. *Gels*, **8**(9), 599 (2022).
63. Šeperienė, N. *The Development of Polymer Gels and Composites with the Enhanced Sensitivity To low-dose Irradiation* (Kauno technologijos universitetas, 2018).
64. Trabelsi, Y., Benali, N., Bouazzi, Y. & Kanzari, M. Microwave transmission through one-dimensional hybrid quasi-regular (Fibonacci and Thue-Morse)/periodic structures. *Photonic Sens.* **3**, 246–255. https://doi.org/10.1007/s13320-013-0114-7 (2013).
65. Zaghdoudi, J., Maaloul, N. & Kanzari, M. Studies of optical properties of symmetrical quasi-periodic photonic crystals. *Opt. Photon J.* **2**, 270–277. https://doi.org/10.4236/opj.2012.24033 (2012).
66. Silva, B. P. & Costa, C. H. Tuning band structures of photonic multilayers with positive and negative refractive index materials according to generalized fibonacci and Thue–Morse sequences. *J. Phys.: Condens. Matter.* **32**, 135703. https://doi.org/10.1088/1361-648X/ab5ea2 (2019).
67. Singh, S. B., Singh, N. B. & Sharma, H. B. Study on the effect of thickness on structural and optical properties of nanocrystalline bismuth ferrite (BiFeO3) thin films. *Adv. Mater. Res.* **410**, 142–147. https://doi.org/10.4028/www.scientific.net/AMR.410.142 (2012).
68. Kherodia, A. & Panchal, A. K. Analysis of thickness-dependent optical parameters of a-Si: H/nc-Si: H multilayer thin films. *Mater. Renew. Sustainable Energy*. **6**, 1–6. https://doi.org/10.1007/s40243-017-0107-3 (2017).
69. Segovia-Chaves, F. & Taya, S. A. Defect mode tunability for escherichia coli in one-dimensional photonic crystals with thin graphene layers. *Int. J. Mod. Phys. B*. **36**, 2250158. https://doi.org/10.1142/S0217979222501582 (2022).
70. Abd-Elrahman, M., Hafiz, M. M., Qasem, A. & Abdel-Rahim, M. Characterization of the optical constants and dispersion parameters of chalcogenide Te 40 se 30 S 30 thin film: thickness effect. *Appl. Phys. A*. **122**, 1–6. https://doi.org/10.1007/s00339-015-9578-1 (2016).
71. Abdi-Ghaleh, R. & Asad, M. Design of one-dimensional magnetophotonic crystals operating at visible wavelengths. *Eur. Phys. J. D*. **69**, 1–7. https://doi.org/10.1140/epjd/e2014-50618-0 (2015).
72. Esposito, F., Srivastava, A., Campopiano, S. & Iadicicco, A. Radiation effects on long period fiber gratings: A review, *Sensors*, vol. 20, p. 2729, (2020). https://doi.org/10.3390/s20092729
73. Bich, T., Mallam, S., Diso, D., Hotoro, M. & DETERMINATION OF THRESHOLD RADIATION DOSE IN THE DEGRADATION PROCESS OF INDIGO DYE BY GAMMA IRRADIATION TECHNIQUE,. *J. Phys. Sci. Innov. Volume*, **5**, 15–22, (2013).
74. Kher, S., Chaubey, S., Kashyap, R. & Oak, S. M. Turnaround-point long-period fiber gratings (TAP-LPGs) as high-radiation-dose sensors. *IEEE Photonics Technol. Lett.* **24**, 742–744. https://doi.org/10.1109/LPT.2012.2187637 (2012).
75. Stăncălie, A. et al. Long period gratings in unconventional fibers for possible use as radiation dosimeter in high-dose applications. *Sens. Actuators A: Phys.* **271**, 223–229. https://doi.org/10.1016/j.sna.2018.01.034 (2018).

Acknowledgements

The authors are thankful to the Deanship of Graduate Studies and Scientific Research at University of Bisha for supporting this work through the Fast-Track Research Support Program. The authors acknowledge Princess Nourah bint Abdulrahman University Researchers Supporting Project number (PNURSP2025R737), Princess Nourah bint Abdulrahman University, Riyadh, Saudi Arabia.

Author contributions

Z.A. Zaky invented the original idea of the study, implemented the computer code, performed the numerical simulations, analyzed the data, wrote and revised the main manuscript text, and was the team leader. F. A. Sayed analyzed the data, wrote and revised the main manuscript text. May Bin-Jumah analyzed the data and discussed the results. A. H. Aly analyzed the data and discussed the results, M. Sallah analyzed the data and discussed the results. Finally, all Authors developed the final manuscript.

Declarations

Competing interests

The authors declare no competing interests.

Ethics declarations

This article does not contain any studies involving animals or human participants performed by any authors.

Additional information

Correspondence and requests for materials should be addressed to Z.A.Z.

Reprints and permissions information is available at www.nature.com/reprints.